

9/1/2005

## **Climate Sensitivity of Moderate and Low Resolution Versions of CCSM3 to Preindustrial Forcings**

Bette L. Otto-Bliesner<sup>1</sup>, Robert Tomas<sup>1</sup>, Esther C. Brady<sup>1</sup>, Caspar Ammann<sup>1</sup>,  
Zav Kothavala<sup>1</sup>, and Gabriel Clauzet<sup>2</sup>

1 National Center for Atmospheric Research, Boulder, Colorado

2 Department of Physical Oceanography, University of São Paulo, São Paulo, Brazil

Corresponding address, email and telephone numbers:

Dr. Bette Otto-Bliesner  
CCR/CGD  
National Center for Atmospheric Research  
P. O. Box 3000  
Boulder, CO 80307-3000  
Phone: 303-497-1723, Fax: 303-497-1348  
Email: ottobli@ucar.edu

For JCLI CCSM Special Issue

## **Abstract**

Preindustrial (PI) simulations of CCSM3 at two resolutions, a moderate resolution and a low resolution, are described and compared to the standard controls for present-day (PD). Because of computational efficiency, the moderate and low resolution versions of CCSM3 may be appropriate for climate change studies requiring simulations of the order of hundreds to thousands of years. The PI simulations provide the basis for comparison for proxy records that represent average late Holocene conditions.

When forced with preindustrial trace gases, aerosols, and solar irradiance estimates, both resolutions have a global cooling of 1.2-1.3°C, increased sea ice in both hemispheres, and less precipitation near the equator and at mid-latitudes as compared to simulations using present-day forcing. The response to PI forcings differs in the two resolutions for North Atlantic meridional overturning circulation (MOC), the Antarctic Circumpolar Current (ACC), and ENSO. The moderate resolution CCSM3 has enhanced ACC, North Atlantic MOC, and tropical Pacific ENSO variability for PI forcings as compared to PD. The low resolution CCSM3 with more extensive sea ice and colder climate at high northern latitudes in the PD simulation shows less sensitivity of the North Atlantic MOC to PI forcing. ENSO variability and the strength of the ACC do not increase with PI forcing in the low resolution CCSM3.

## 1. Introduction

Climate has been changing since the beginning of the Industrial Revolution. Crutzen (2002) designates the last two centuries starting at 1800 A.D. the “Anthropocene,” to emphasize the important impact of human activities on the Earth and atmosphere. Since 1800 A.D., atmospheric carbon dioxide (CO<sub>2</sub>) concentration has increased by more than 30% and atmospheric methane (CH<sub>4</sub>) has doubled, resulting in a net radiative forcing for greenhouse gases changes of more than 1.5 W m<sup>-2</sup> (Ramaswamy *et al.*, 2001). Instrumental and proxy records indicate that the Northern Hemisphere mean surface temperature has increased by approximately 0.6-0.9°C over the 20<sup>th</sup> century and roughly 1°C since 1800 A.D. (Jones and Mann, 2004).

Understanding climates farther back in time provides tests of our understanding of climate change and our ability to model this change and the extreme states of the climate system. Estimating the climate states for these past periods requires calibrating and dating proxy indicators, such as tree rings or layered sediments recovered from ocean, lake, or ice cores, to observed climate variables. For lower resolution records such as ocean sediment cores and pollen, the record may represent decadal to centennial means. Thus, these records represent the mean climate for preindustrial or late Holocene conditions rather than present climate. In this study, we therefore consider climate simulated for average PI forcings and discuss differences in the simulations of two versions of CCSM3 available to the community.

This paper compares the mean climate states for preindustrial and present conditions for two different versions of CCSM3. The versions differ in their horizontal grids, applying low- and moderate-resolution configurations that may be useful for studies of past climates because of their computational efficiencies. Additionally, results from a simplified version

of CCSM3 where a simple ‘slab’ ocean has replaced the three-dimensional ocean are shown. Differences of the mean climate are discussed for the atmosphere, ocean, and sea ice. Changes to interannual and decadal variability of the tropical Pacific region, the Arctic, and the southern high latitudes are also described.

## **2. Model description and forcings**

The NCAR CCSM3 is a global, coupled ocean/atmosphere/sea ice/land surface climate model. Model details are given elsewhere in this issue (Collins *et al.*, 2005a). Briefly, the atmospheric model is the NCAR CAM3, which is a three-dimensional primitive equation model solved with the spectral method in the horizontal (Collins *et al.*, 2005b). The ocean model is the NCAR implementation of POP (Parallel Ocean Program) and is a three-dimensional primitive equation model in spherical polar coordinates with vertical z-coordinate (Gent *et al.*, 2005). The sea ice model is a dynamic-thermodynamic model, which includes a subgrid-scale ice thickness parameterization and elastic-viscous-plastic rheology (Briegleb *et al.*, 2004). The land model includes a river routing scheme and specified land cover and plant functional types (Dickinson *et al.*, 2005).

### *a. Resolutions*

For these simulations, two atmospheric resolutions are used: T42 (an equivalent grid spacing of approximately  $2.8^\circ$  in latitude and longitude) and T31 (an equivalent grid spacing of approximately  $3.75^\circ$  in latitude and longitude). Both resolutions have 26 levels in the vertical, which are unevenly spaced and are terrain-following. The land surface grid matches the atmospheric grid but allows for multiple land cover and vegetation types within a grid

cell. The cloud process parameterization scheme is adjusted between the T42 and T31 atmosphere models to improve top-of-atmosphere energy budget (Hack *et al.*, 2005a).

The ocean/sea ice grids used are the x1 (320x384 points and 40 levels to 5.5 km depth) and the x3 (100x116 points and 25 levels to 5 km depth). Both ocean/sea ice grids locate the poles in Greenland and Antarctica. The horizontal resolutions correspond to a nominal grid spacing of approximately 1° and 3° in latitude and longitude with significantly greater resolution in the tropics and North Atlantic. The x1 and x3 ocean vertical grids are constructed to have similar vertical resolution in the top 50 m. In addition, the x3 version of the ocean model excludes the parameterization for the diurnal solar cycle and uses a centered-difference ocean advection scheme instead of the upwinding used in the x1 version. These parameterization changes improve simulation of ENSO and the western equatorial Pacific in the x3 version of CCSM3. Snow and ice albedos over sea ice are lowered by 6-9% in the x3 version of the model as compared to the x1 version (Yeager *et al.*, 2005).

The coupled simulations discussed in this paper are with CCSM3 at moderate resolution, T42 atmosphere/land grid coupled with the x1 ocean/sea ice grid (termed T42x1), and at low resolution, T31 atmosphere/land grid coupled with the x3 ocean/sea ice grid (termed T31x3). A computationally less expensive means of evaluating climate changes is to replace the three-dimensional ocean model with a slab ocean model (SOM) with prescribed ocean heat transports. This is the standard method to compare the climate sensitivity of different models to a doubling of atmospheric CO<sub>2</sub>. Here, we also show the sensitivity of annual temperature, the Arctic Oscillation, and Southern Annular Mode in a T42 SOM simulation to the same PI forcings as the coupled model simulations. The prescribed ocean

heat transports and mixed layer depths are the same in the PI and PD simulations with the T42 SOM model (Kiehl *et al.*, 2005).

*b. Preindustrial boundary conditions*

The specified PI forcings follow the protocols of the Paleoclimate Modeling Intercomparison Project, Phase 2 (PMIP-2) [<http://www-lsce.cea.fr/pmip2/>]. These include reduced concentrations of the well-mixed greenhouse gases, changes in the spatial distributions of ozone, sulfate (only direct effect), and carbonaceous aerosol, as well as a reduced solar constant. These forcings represent the average conditions of the late Holocene before the significant impact of humans rather than a specific date. Table 1 summarizes the individual specifications.

Estimates of the changes in radiative forcing (PI minus PD) due to reductions in the greenhouse gases on the troposphere can be calculated with formula in the 2001 IPCC report (Ramaswamy *et al.*, 2001). The greenhouse gas radiative forcing changes are all negative with a net change of  $-2.05 \text{ W m}^{-2}$  for the PI forcings. The largest contribution is from lowering of  $\text{CO}_2$  concentration, followed by methane, which is about a third as large.  $\text{N}_2\text{O}$  and CFC changes contribute an additional  $-0.35 \text{ W m}^{-2}$  forcing to the troposphere. The reduction of the solar constant of  $2 \text{ W m}^{-2}$  at the top of the atmosphere perturbs the system by  $-0.35 \text{ W m}^{-2}$ .

Atmospheric ozone distributions are prescribed using an ozone climatology from measurements for PD (Wang *et al.*, 1995) and from MOZART simulations for PI (Lamarque *et al.*, 2005). Tropospheric ozone increases by 8.3 Db from PI to PD and total ozone increases by 10.2 Db for the same period. Sulfate and carbonaceous aerosols have increased with industrialization. For the PI simulations, the distribution of sources of carbonaceous

aerosols is assumed to be unchanged from present but the magnitude is reduced to 30% of present-day based upon scaling by the population. Dust and sea salt aerosols are assumed to be the same as present-day (Collins *et al.*, 2005b). The distribution and magnitude of PI sulfate aerosols are derived using specified 1870 A.D. sources (Smith *et al.*, 2001) and modeling of sinks and atmospheric sulfate transport (Barth *et al.*, 2000; Rasch *et al.*, 2000).

### **3. Mean climate**

The PD simulations are described elsewhere in this issue (Hack *et al.*, 2005b; Large and Danabasoglu, 2005; Yeager *et al.*, 2005; Holland *et al.*, 2005). The PI simulations are branched from PD simulations and run an additional 400 years. Northern Hemisphere and tropical climates equilibrate in 100-200 years for both resolutions. Southern Hemisphere SSTs and sea ice still exhibit trends after 400 years, but these trends are small, less than 0.1°C and 1%, respectively. The mean climate results compare averages for the last 50 years of the PI simulations to the corresponding 50 years of the PD simulations, except as noted when longer averages are needed to yield stable statistics. The Student t-test is used to evaluate the significance of differences between the PI and PD simulations of atmospheric variables.

#### *a. Atmosphere changes*

##### **1) SURFACE TEMPERATURE**

The global and annually averaged surface temperature is 13.5°C in the T42x1 PI simulation, a cooling of 1.3°C compared to present (Table 2). The T31x3 PI simulation is colder than the T42x1 PI simulation with the global and annually averaged surface temperature of 12.8°C, but has a similar cooling compared to present of 1.2°C.

The PI zonal distributions of cooling simulated by T42x1 and T31x3 CCSM3 are statistically different than PD at all latitudes (Fig. 1). The magnitudes of cooling are statistically similar in the two resolutions except at high northern latitudes. Cooling in the tropics and subtropics is  $\sim 1^\circ\text{C}$  with slightly greater cooling over the continents ( $1.2^\circ\text{C}$ ) than the adjoining oceans ( $0.9^\circ\text{C}$ ) (Table 2). Cooling over Antarctica and the southern oceans averages  $1\text{-}2^\circ\text{C}$ . The largest PI cooling relative to PD in both resolutions occurs at high northern latitudes and is significantly greater at T42x1 resolution, with cooling greater than  $4^\circ\text{C}$  at latitudes poleward of  $\sim 75^\circ\text{N}$ . The greater sensitivity in the T42x1 simulation is associated with a greater change of NH sea ice with PI forcings (Table 2), and is ultimately associated with the more realistic NH sea ice distribution simulated for PD at T42x1 versus T31x3 resolution (Yeager *et al.*, 2005).

The T42-SOM model simulates greater cooling in the tropics and southern high latitudes and less cooling at northern high latitudes than in the fully coupled model for PI forcings (Fig. 1). Equatorial surface temperatures are  $\sim 0.5^\circ\text{C}$  cooler in the SOM PI simulation than the coupled PI simulation, and exhibit a hemispheric asymmetry with cooling less in the northern tropics than southern tropics. Cooling at high southern latitudes is  $3\text{-}4^\circ\text{C}$  in the SOM simulation as compared to  $\sim 1.5^\circ\text{C}$  in the coupled simulation. The SOM simulations with prescribed OHT and more realistic PD distribution of sea ice in both hemispheres have smaller increases in sea ice in the NH ( $10.3$  to  $11.3 \times 10^6 \text{ km}^2$ ) and greater increases in the SH ( $8.7$  to  $14.8 \times 10^6 \text{ km}^2$ ) for PD to PI conditions.

## 2) SURFACE HEAT FLUXES

The surface heat fluxes (Table 2) change in the PI simulations in response to the cooling. Both net shortwave absorbed and net longwave emitted at the surface increase

under PI forcing, primarily at low latitudes between 30°N-30°S. These changes are tied to both reduced atmospheric aerosols and a drier atmosphere in the PI simulations. As expected for the cooler climate of the PI simulations, the amount of precipitable water in the atmosphere is significantly less at all latitudes with decreases near the equator in excess of 4 mm or about 10% of the total precipitable water. The partitioning between latent and sensible heat fluxes from the surface is also altered under PI forcing, with decreased global latent heat flux with cooler surface temperatures but increased sensible heat flux. Although the T42x1 PI and T31x3 PI simulations show comparable changes in the surface heat fluxes, the T42x1 PI simulation has significantly greater latent heat flux and statistically significant less sensible heat flux than the T31x3 PI simulation.

### 3) PRECIPITATION

Global and annually averaged precipitation is 2.74 mm/day (1000 mm/year) for the T42x1 PI simulation and 2.66 mm/day (971 mm/year) for the T31x3 PI simulation (Table 2). Both PI simulations have maximum precipitation rates in the western Pacific warm pool extending into the Indian Ocean, over equatorial central and western Africa extending into the eastern Atlantic, and just south of the equator in South America (Fig. 2). Over the central and eastern Pacific equatorial ocean, maximum precipitation occurs just north and south of the equator with a dry tongue over the equator. The dry tongue extends slightly farther west in the T42x1 PI simulation than the T31x3 PI simulation, as was also true in the previous version of the model CSM1 (Otto-Bliesner and Brady, 2001). The T42x1 PI simulation shows more intense precipitation in the northern Atlantic and Pacific storm tracks than the T31x3 PI simulation as well as enhanced drying associated with the subtropical highs of both

hemispheres. Precipitation associated with the ITCZ is also greater in the T42x1 PI simulation.

The PI simulations show only slight decreases (-0.05 mm/day) in precipitation on a global and annually basis as compared to the PD simulations, with greater decreases over land than the oceans (Table 2). Significant decreases in precipitation occur at middle to high latitudes in both hemispheres and in the tropics with the largest decreases at  $\sim 5^{\circ}\text{N}$ , for both PI simulations as compared to PD (Fig. 2).

#### 4) SEA LEVEL PRESSURE

The mean features of the December-January-February (DJF) sea level pressure field, the Aleutian and Icelandic Lows and seasonal continental highs in the NH and Antarctic circumpolar low pressure belt, subtropical oceanic highs, and seasonal low pressure over Australia and South America in the SH, have a similar distribution in the T42x1 and T31x3 PI simulations, but differ in intensity (Fig. 3). The T42x1 PI simulation has a more intense Icelandic Low in DJF than the T31x3 PI simulation (988 vs. 993 mb) and this low extends farther northeast in the T42x1 simulation. The intensity and spatial extent of the Aleutian low is similar between the two resolutions. High pressure over the northern subtropical oceans is more intense in the T42x1 PI simulations than the T31x3 PI simulation. In the Southern Hemisphere, in both DJF and June-July-August (JJA), the subtropical highs are more intense and the Antarctic circumpolar low-pressure belt is 5 mb deeper in the T42x1 PI simulation as compared to the T31x3 PI simulation. This results in the T42x1 PI simulation having a stronger meridional pressure gradient than the T31x3 PI simulations. Maximum annual zonal wind stresses associated with the mid-latitude SH pressure gradient are  $0.22 \text{ N m}^{-2}$  at  $48^{\circ}\text{S}$  in the T42x1 PI simulation compared to  $0.18 \text{ N m}^{-2}$  at  $42^{\circ}\text{S}$  in the T31x3 PI simulation.

Compared to the PD simulations, both resolutions show increases in DJF sea level pressure in the North Pacific-Bering Strait region, but for the T42x1 PI simulation this increase is associated with a significant filling of the Aleutian Low, while for the T31x3 PI simulation, the sea level pressure increases are associated with a southward shift of the Aleutian Low. Both resolutions also show significant changes in the Southern Hemisphere pressure features. In particular, the PI simulations have a weakening of the DJF SH subtropical highs and subpolar low-pressure belt compared to present. This weakening is more pronounced in the T42x1 PI simulation. Changes in JJA sea level pressure patterns between the PI and PD simulations are much smaller.

*b. Ocean changes*

1) EQUATORIAL UPPER OCEAN POTENTIAL TEMPERATURE

The annually averaged equatorial potential temperature profiles show significant resolution dependence to PI forcing (Fig. 4). The T31x3 PI simulation has a shallower upper equatorial thermocline by ~15m and colder potential temperatures at all depths to 800m in the central Pacific compared to the T42x1 PI simulation. On the western boundary of the Pacific, both the T31x3 and T42x1 PI simulations have a shallower thermocline as measured by the depth of the 20°C isotherm compared to observations (Kessler, 1990).

The equatorial thermocline has similar sharpness in the T31x3 PI simulation as in the T42x1 PI simulation. This is surprising considering the lower horizontal resolution in the T31x3 ocean component and the slightly lower vertical resolution in the upper 200m of the T31x3 ocean component (11 vertical levels in the T31x3 compared to 14 in the T42x1). A factor giving greater sharpness in the T31x3 ocean model is the use of a centered finite difference advection scheme instead of the more diffusive third-order upwinding scheme

used in the T42x1 ocean model. In addition, the diurnal cycle of solar forcing option is turned off in the T31x3 model.

The cooling of the Pacific in the T42x1 PI simulation compared to PD is greater near the surface than the cooling noted in the T31x3 PI-PD comparison. Slightly greater cooling is noted in the Atlantic basin both at the surface and at depth in the T42x1 PI-PD comparison than the T31x3 PI-PD comparison. In the Indian Ocean, there is a notable warming along the western boundary below 200 m in the T31x3 PI simulation compared to PD, which is not as apparent in the moderate resolution simulation. This warming is associated with the southward spread along the western boundary of warmer and more saline water associated with greater net freshwater deficit in the Arabian Sea in the T31x3 PI simulation compared to PD. A similar large warm (and salty) bias shows up in the T31x3 PD simulation as compared to Levitus.

## 2) MASS TRANSPORTS

In general, the transports through key straits (Table 3) are weaker than observed estimates in the T31x3 PI simulation and similar to observed estimates in the T42x1 PI simulation with the exception of the ACC transport through the Drake Passage (DP). The ACC transport is much larger than present day observed estimates (Whitworth and Peterson, 1985) by about 50-65Sv in the T42x1 PI simulation and too weak by about 15 Sv in the T31x3 PI simulation. Gent *et al.* (2001) showed that Drake Passage transport in numerical models is strongly dependent on both zonal wind stress forcing in the Drake Passage and thermohaline circulation off the Antarctic shelf forced by brine rejection in sea ice formation. In the T31x3 PI simulation, the zonal wind stress at the latitude of the DP is notably weaker than the T42x1 PI simulation due to an equatorward shift of the maximum westerlies in the

T31x3 simulation relative to the T42x1 simulation. There is also a notable enhancement of SH sea-ice formation in the T42x1 PI simulation.

The ACC transports in the T42x1 and T31x3 simulations show different sensitivity to PI forcing. In the T42x1 PI simulation, ACC transport increases by 16 Sv from the PD simulation. In the T31x1 PI and PD simulations, the mean ACC transport is similar in magnitude. Both resolutions show a weakening and slight equatorward shift of the westerly wind stress in the Southern Ocean. By itself, this should lead to a decrease in the ACC transport. However, there is an enhancement in sea-ice formation at PI compared to PD forcing at both T42x1 and T31x3 resolution. The two forcing mechanisms of the ACC oppose more equally in the T31x3 PI simulation producing a reduced sensitivity in the ACC transport. In the T42x1 PI simulation, the ACC transport is much more sensitive to sea-ice formation. The Pacific Indonesian Throughflow, Florida Straits, and Bering Strait transports are all slightly larger in both PI simulations compared to the PD simulations, however the differences are small.

The strength and depth of the maximum meridional overturning streamfunction in the Atlantic basin of the PI simulations shows some resolution dependence (Fig. 5, Table 3). The T42x1 PI simulation transports about 25% more warm surface water poleward at the maximum than the T31x3 PI simulation. This warm water is transformed into North Atlantic Deep Water (NADW) through buoyancy loss in the high latitude regions. Twice as much sinks north of 60°N in the T42x1 simulation than in the T31x3 simulation. The maximum meridional overturning streamfunction associated with NADW formation is deeper in the T42x1 PI simulation at 1022m than the T31x3 simulation at 944m. There is indication that the maximum meridional overturning streamfunction is shifted poleward in the T42x1

simulation by about a degree latitude. There is only a small difference in the strength of the Antarctic Bottom water (ABW) transported into the South Atlantic (Table 3) however the ABW cell is stronger in the T42x1 simulation.

Both resolutions show significant differences between the PI and PD climate forcings (Fig. 5, Table 3). However, these differences are notably weaker in the T31x3 simulation. Both resolutions show that the NADW overturning cell is stronger and penetrates deeper with PI forcing compared to PD forcing and the ABW cell is stronger with PI forcing. This result agrees with the trends and patterns of change due to transient CO<sub>2</sub> forcing shown by Bryan et al. (Bryan *et al.*, 2005). The overall pattern of change is similar in both resolutions with the maximum difference located below the maximum overturning of NADW. However, the maximum overturning of NADW strengthened to a greater extent with PI forcing in the T42x1 resolution compared to the T31x3 resolution.

### 3) HEAT TRANSPORT

The latitudinal profiles of Atlantic ocean heat transport show heat transported northward in both hemispheres (Fig. 6). The maximum northward heat transport occurs at ~20°N for all forcings and resolutions. The T31x3 PI and PD ocean components transport similar amounts of heat northward in the Atlantic. The T42x1 PI simulation shows a slightly higher ocean heat transport in the North Atlantic between the equator and 50°N than the T42x1 PD simulation. Much larger differences exist between the T42x1 and T31x3 PI simulations. The T42x1 PI simulation transports more heat northward in the Atlantic basin, accounting for the larger global northward heat transport than the T31x3 PI simulation. This is related to the stronger meridional overturning (about 30% greater) in the Atlantic in the T42x1 PI simulation as compared to the T31x3 PI simulation.

### *c. Sea ice changes*

#### 1) NORTHERN HEMISPHERE DISTRIBUTION

The greatest sea ice thicknesses in the NH in both PI simulations are located over the Arctic Ocean, with local maxima located between 150°E and the dateline, in a narrow strip along the east coast of Greenland, and in Baffin Bay northwest of Greenland (Fig. 7). During the February-March, thicknesses in these locations range from 3-4 meters up to 6-7 meters. Also during the northern winter season, relatively thinner ice with thickness values from 0.25 to several meters extend southward, into the Labrador and Greenland Seas and in the Pacific sector into the Bering Sea and down to the northern tip of Japan. The T31x3 PI simulation has sea ice covering the Barents Sea in February-March. This region is ice-free in the T42x1 PI simulation. During August-September, the thinner ice retreats poleward leaving the southern regions ice-free (less than 0.25 m). The higher latitudes remain ice covered during the summer season; however thickness values are 1 to 2 meters less than during the winter.

In both of the T42x1 and T31x3 PI simulations, the ice is thicker compared to the corresponding PD simulation, with the greatest changes located north of Greenland and extending over much of the Arctic Ocean, along the east coast of Greenland to near the southern most point, and to the northwest of Greenland. Although even PD conditions are somewhat overestimated, especially around southern Greenland and the Labrador Sea, higher sea ice concentrations and increased thickness can be expected for the cooler climates of the PI. The T42x1 PI simulation also has significantly more sea ice than PD off Newfoundland. Close examination of these diagrams reveals that the T31x3 PI and PD simulations have more ice than the T42x1 PI and PD simulations in the NH during both the winter and summer seasons.

## 2) SOUTHERN HEMISPHERE DISTRIBUTION

In the SH, the largest ice thickness values are located in the oceans along the Antarctic coast, with an unrealistically large local maximum in excess of 7 meters in the Weddell Sea (Fig. 7). Seasonal changes in the ice thickness distribution occur primarily in those regions covered by ice less than 3 meters thick. During August-September, sea ice is located as far equatorward as 50-55° latitude in the South Atlantic and Indian oceans in the T42x1 PI simulation. A similar distribution, though not quite as extensive, is found in the T31x3 PI simulation. The similarity between the ice thickness distribution for the T42x1 and T31x3 PI simulation. The similarity between the ice thickness distribution for the T42x1 and T31x3 simulations is closer in the SH than it is in the NH. As in the NH, the T42x1 PI simulation has greater increases (~1 meter) in ice thickness from PD than the T31x3 PI simulation. The largest values in the difference fields are located where there are maxima in the thickness.

## 3) SEASONAL CYCLE

The seasonal cycle of the aggregate sea ice area for the two PI simulations shows that the most extensive sea ice for the NH occurs in the T31x3 PI simulation and for the SH in the T42x1 PI simulation (Fig. 8, Table 2). This is consistent with the ice thickness distributions. For the PI and PD simulations at both resolutions, the wintertime values are about twice those during summertime in the NH and about three times in the SH. The increase in ice area for the PI case compared to the PD case is slightly greater at T42x1 than it is for T31x3 resolution. Note that the seasonal cycle of sea ice area for the T31x3 PD simulation closely matches the one for the T42x1 PI simulation in the NH during all months of the year.

## 4. Interannual and decadal variability

Patterns of climate variability and their influence on regional climates provide for predictability of the climate system on multi-monthly to multi-annual time scales. During the last decades, there has been a substantial effort toward understanding whether the recent observed climate variations are induced by anthropogenic forcing or are part of the natural variability of our climate system. Important for this assessment is whether patterns, amplitudes, and time variations of interannual-decadal variability have changed in the recent past (Cobb *et al.*, 2003; Cook *et al.*, 2002).

For the PI simulations, we discuss three patterns or modes of variability that have been identified as important for explaining a large fraction of regional variability on interannual to decadal time scales. The El Niño – Southern Oscillation (ENSO) mode of variability is tied to coupled atmosphere-ocean interactions in the tropical Pacific region. The Northern Annular Mode (NAM) or Arctic Oscillation (AO) and Southern Annular Mode (SAM) or Antarctic Oscillation (AAO) are modes of pressure variation circling the north and south poles, respectively. The last 100 years are analyzed for the AO and SAM and last 350 years for ENSO.

*a. Tropical Pacific variability*

The ENSO variabilities in the T42x1 and T31x3 coupled models differ with respect to the seasonal phase characteristics, amplitude, and sensitivity to PI forcing (Fig. 9, Table 3). The T31x3 version of the CCSM3 exhibits weaker amplitude of ENSO variability as defined by the standard deviation of SST anomalies averaged over the Niño3.4 region. The T31x3 PI and PD simulations both show a standard deviation of Niño3.4 of  $\sim 0.7^{\circ}\text{C}$ , indicating a relatively weak ENSO compared to observed and little sensitivity of the Niño3.4 amplitude to the PI forcing. The T42x1 PI and PD simulations have larger ENSO variability, with

standard deviations of Niño3.4 of 0.84 and 0.74°C, respectively. This difference is statistically significant at the 90% level. The observed Niño3.4 computed from 1948-2003 NCEP reanalysis data is 0.82°C.

The T31x3 simulations also show a weaker and degraded phasing of the seasonal cycle of monthly Niño3.4 compared to the T42x1 simulations. The annual cycles of Niño3.4 for the T42x1 simulations show a peak in variability in the November-January and a minimum in March-May, in accord with observations (Deser *et al.*, 2005). Contrary to these observations, Niño3.4 SST variability in the T31x3 simulations peaks in the boreal fall months (August-November). Comparing the seasonal cycles of Niño3.4 in the PI simulations to the PD simulations, only the T42x1 PI simulation is significantly different at the 95% confidence level. The T42x1 PI simulation exhibits statistically significant higher Niño3.4 variability in boreal winter months of December- March than the T42x1 PD simulation. All cases show similar levels of variability in boreal spring.

#### *b. Arctic Oscillation*

The Arctic Oscillation (AO) is defined as the first empirical orthogonal function (EOF) of sea level pressure in boreal winter (December-January-February-March [DJFM]) from 20-90°N. It is the dominant pattern of non-seasonal variations of sea level pressure at middle and high latitudes in the Northern Hemisphere.

Both PI simulations exhibit similar AO patterns with sea level pressures of one sign circling the globe at ~45°N and sea level pressures of the opposite sign over polar latitudes (Fig. 10). The AO explains 35% of the total variance in the T42x1 PI simulation and 37% of the total variance in the T31x3 PI simulation. Similar to the PD simulations, the mid-latitude variability has two centers of action: one over the North Pacific with greatest variability east

of the dateline and one over the North Atlantic with greatest variability in southern Europe. Variability at polar latitudes is greatest between Greenland and Iceland. Both resolutions exhibit larger amplitudes of the Pacific ridge of AO variability than observed. This bias is also present in the CAM3 atmosphere simulation with prescribed SSTs, suggesting it is mainly associated with the atmosphere and not air-sea coupling (Hurrell *et al.*, 2005). Similar to present observed correlations (Thompson and Wallace, 1998), during high (positive) AO years in the PI winters, northern Europe and Asia experience above average temperatures and precipitation (not shown), southern Europe has below average precipitation, the Labrador Sea region is cooler and drier, and the southeastern US is warmer (Fig. 10).

The T42 SOM PI simulation displays the same overall pattern of AO variability in DJFM as the coupled run (Fig. 10). Differences include a shift in the node line poleward over the North Atlantic, and north of this transition, a shift eastward of the maximum variability from the Greenland-Iceland region to northern Eurasia. Associated with this shift, surface temperature regressions in Scandinavia are weaker than the coupled model.

The spectrum of the AO for the T42x1 PI and T42-SOM PI simulations both show roughly the same total variability, as indicated by the area under the curves, and the same degree of enhanced low frequency variability or redness. These behaviors are consistent with the SOM having thermal inertia properties similar to those of the full ocean model, at least with regard to how this property affects the time dependence of the AO (Deser *et al.*, 2003). The spectrum of the AO for the T31x3 PI simulation shows less total variability and is whiter than the T42x1 PI simulation. Error bars based on chi-squared statistics show the difference in low frequency variability between the two resolutions to be statistically significant at or above the 95% level. This resolution dependence may be a consequence of differences

between the mixed layers in the two coupled simulations. The annually-averaged mixed layer depths in the T31x3 PI simulation are shallower than in the higher resolution simulation. None of the spectra shown for the AO contain statistically significant peaks when compared to the appropriate background spectra based on a red noise time series.

*c. Southern Annular Mode*

The Southern Annular Mode (SAM) or Antarctic Oscillation (AAO) is defined as the first EOF of sea level pressure from 20-90°S (Gong and Wang, 1998). In this study, the monthly mean sea level pressures are used. In the PI simulations, the SAM accounts for a significant part of the total variance, 36% in T42x1 and 37% in T31x3. Both PI simulations exhibit similar SAM patterns, with a strong zonally symmetric component, showing an out-of-phase relationship of sea level pressure between the Antarctic and mid-latitudes at all longitudes (Fig. 11). A center of minimum variability occurs near the Bellingshausen Sea region. During high SAM years in the PI simulation, the Antarctic continent is colder and drier except for the Antarctic Peninsula which is warmer and wetter, New Zealand and the southern tip of South America are warmer and drier, and Australia and South Africa are cooler and wetter (not shown). Surface temperature changes associated with the SAM are weaker in the T31x3 PI simulation than the T42x1 PI simulation.

None of the model spectra for the SAM contain statistically significant peaks when compared to the appropriate background spectra based on a red noise time series. The spectrum of the SAM index for the T42x1 PI, T42-SOM PI and T31x3 PI cases behave differently than their counterparts in the Northern Hemisphere. The T42x1 PI spectrum contains more total variability and is redder than the T42-SOM PI simulation. This may also be related to differences in the thermal inertia effects of the slab ocean compared to

the full ocean model. As in the NH case, there is resolution dependence, with the T31x3 PI spectrum showing considerably less total variability than the T42x1 PI spectrum. There is also considerably less low frequency variability in the low resolution simulation and this is statistically significant at or above the 95% level. Annual mean mixed layer depths for the T31x3 PI simulation are shallower than the higher resolution case.

## **5. Discussion**

### *a. Coupled climate response of T42x1 CCSM3 to PI forcing*

At high northern latitudes, the T42x1 PI simulation has a large polar amplification of cooling as compared to the PD simulation, with annual surface cooling in excess of 5°C near the North Pole, primarily associated with the winter season. Northern Hemisphere sea ice is thicker, its area extent increases by 20%, and its seasonal cycle is enhanced. In association with the enhanced temperature gradient at PI, the ocean heat transport increases in the North Atlantic from the equator to 50°N and the North Atlantic meridional overturning circulation increases by 10% (although this feature has large interannual variability). Cooling of the surface ocean is distributed to depth in the North Atlantic by the overturning circulation. High latitude dynamical features, in particular the Icelandic Low and the Arctic Oscillation, show no significant adjustment to the changed PI forcing.

At high southern latitudes, the cooling in the T42x1 PI simulation is smaller, on average about 1.5°C. Southern Hemisphere sea ice increases in thickness and in area extent by 15%, and its seasonal cycle is enhanced with greater sea ice increases in the austral winter than summer. In contrast to the high northern latitudes, the atmospheric circulations at high southern latitudes exhibit significant changes in strength at PI as compared to PD. The subtropical high pressure belt at ~35°S and the Antarctic circumpolar low pressure belt at

60°S both weaken resulting in a weaker pressure gradient and weaker surface zonal wind stresses. The mass transport through the Drake Passage though increases by 9 % in association with the seasonal sea ice changes and Antarctic Bottom Water production, which is only partially offset by the decreased zonal wind stress.

Tropical surface temperatures in the T42x1 PI simulation cool by ~1°C with greater cooling over land (-1.2°C) than over the oceans (-0.9°C). In the Pacific at the equator, SSTs cool more in the eastern and central Pacific than the western Pacific enhancing the east-west SST gradient, but cool more at the surface than at 200m depth reducing the thermocline intensity. The Niño3.4 variability is enhanced at PI compared to PD, significantly during December-March.

*b. Resolution dependence of climate response to PI forcing*

There are several notable differences in the sensitivity of the low resolution T31x3 CCSM3 to PI forcing as compared to the moderate resolution T42x1 CCSM3. The polar amplification of cooling in the Arctic is smaller in the T31x3 PI simulation with annual surface cooling of only ~3°C near the North Pole. Correspondingly, the North Atlantic ocean heat transport and maximum meridional overturning circulation show less difference from the T31x3 PD simulation. Northern Hemisphere sea ice extent increases by only 10%. This decreased sensitivity is related to the area extent of Northern Hemisphere sea ice in the T31x3 PD simulation being too extensive.

At southern high latitudes, changes between PI and PD in the intensities of the subtropical high pressure belt, the Antarctic circumpolar low pressure belt, the pressure gradient between these features, and the zonal wind stresses are considerably smaller in the T31x3 CCSM3. Mass transport through the Drake Passage is unchanged between the PI and

PD simulations at T31x3 resolution. In the T31x3 simulation for PI conditions, increases in the ACC in association with seasonal sea ice changes and ABW production are compensated by decreases in the ACC due to a weakening and equatorward shift of the westerly wind stress in the Southern Ocean. In the tropics, the Niño3.4 variability peaks too early in boreal fall and shows no sensitivity to PI forcing at T31x3 resolution.

Bryan *et al.* (2005) find significant differences in the mean state of the North Atlantic and its response to global warming in the T31x3 and T42x1 versions of CCSM3. Both resolutions show a reduction in the depth penetration of NADW at time of 4xCO<sub>2</sub> in 1% per year transient increase simulations but the T31x3 has reduced sensitivity. They hypothesize that the reduced sensitivity in the T31x3 CCSM3 as compared to the T42x1 CCSM3 is related to representation of processes in the Greenland-Iceland-Norwegian (GIN) Sea region and the larger PD sea ice extent in the North Atlantic in the T31x3 CCSM3.

CCSM3 has also been shown to have a resolution dependence of climate sensitivity for the equilibrium change in surface temperature for a doubling of atmospheric CO<sub>2</sub>. The climate sensitivity of CAM3 coupled to a slab ocean model is 2.3°C for T31 and 2.5°C for T42 at doubled CO<sub>2</sub>. Kiehl *et al.* (2005) show that the increase in climate sensitivity with increased horizontal resolution is highly correlated with changes in shortwave cloud forcing. Shortwave cloud forcing, which lessens the warming, is  $-0.3 \text{ W m}^{-2}$  larger in the T31 doubled CO<sub>2</sub> CAM3 simulation as compared to the corresponding T42 CAM3 simulation.

### *c. Comparison to proxy indicators*

Direct comparison of the simulated PI climate responses to proxy-based climate reconstructions of the preindustrial period provides a measure of the sensitivity of the models

to modest changes in the mean radiative forcing. Here, we present only a comparison to average changes from PI to PD documented in the literature.

The simulated Northern Hemisphere PD to PI temperature differences of 1.2 and 1.3°C are larger than some proxy reconstructions (Jones and Mann, 2004), but compares favorably to greater cooling in the 17<sup>th</sup>-18<sup>th</sup> centuries shown by other reconstructions (Esper *et al.*, 2002; Huang *et al.*, 2000). Increased sea ice in the North Atlantic simulated by CCSM3 for PI forcings agrees with historical records (Rayner *et al.*, 2003). CCSM3 simulates a cooler and drier tropical Pacific for PI versus PD forcings similar to the record of central tropical Pacific corals, which indicate cooler and drier conditions in previous centuries as compared to the 20<sup>th</sup> century (Cobb *et al.*, 2003; Urban *et al.*, 2000).

## 6. Conclusions

In this paper, we compare the equilibrium climate predicted by CCSM3 for present-day and preindustrial conditions at two resolutions appropriate for paleoclimate studies, a moderate resolution T42x1 useful for runs of several hundred years for past periods when proxy data is abundant and forcings are well constrained, and a low resolution T31x3 useful for transient runs of several thousand years and deep-time paleoclimate investigations. Because of reductions in resolution in all the CCSM3 model components at T31x3 resolution compared to the T42x1 resolution, the T31x3 CCSM3 is faster to run computationally by a factor of ~3-5 times, depending on computing architecture, than that of the T42x1 CCSM3 (Yeager *et al.*, 2005).

The PI simulations are forced with adjusted atmospheric greenhouse gases (CO<sub>2</sub>, CH<sub>4</sub>, N<sub>2</sub>O, CFCs, and ozone), solar constant, and aerosols (tropospheric sulfate and carbonaceous aerosols). The radiative forcing change by well-mixed greenhouse gases of

about  $-2 \text{ W m}^{-2}$  is somewhat offset by the reduced aerosols. The total forcing change remains negative. Significant changes in surface temperature over both land and oceans, precipitation, and sea ice extent for PI conditions as compared to present-day indicate a critical need to understand and document the meaning of “core-top” proxy estimate of these quantities when comparing past climate change anomalies predicted by climate models (Otto-Bliesner *et al.*, 2005).

### **Acknowledgments**

This study is based on model integrations performed by NCAR and CRIEPI with support and facilities provided by NSF and ESC/JAMSTEC. The authors wish to thank the CCSM Software Engineering Group for contributions to the code development and running of simulations and Scott Weese (NCAR) and Dr. Yoshikatsu Yoshida (CRIEPI) for handling of the Earth Simulator simulation. Sylvia Murphy, Mark Stevens, and Adam Phillips provided assistance with the graphics, and Dr. Matthew Huber provided a critical and thoughtful review. These simulations would not have been possible without the dedication of the CCSM scientists and software engineers in the development of CCSM3.

## References

- Barth, M. C., P. J. Rasch, J. T. Kiehl, C. M. Benkovitz, and S. E. Schwartz, 2000: Sulfur chemistry in the National Center for Atmospheric Research Community Climate Model: Description, evaluation, features and sensitivity to aqueous chemistry. *J. Geophys. Res.*, **105**, 1387-1415.
- Briegleb, B. P., C. M. Bitz, E. C. Hunke, W. H. Lipscomb, M. M. Holland, J. L. Schramm, and R. E. Moritz, 2004: Scientific description of the sea ice component in the Community Climate System Model, Version 3, 70 pp.
- Bryan, F. O., G. Danabasoglu, N. Nakashiki, Y. Yoshida, D.-H. Kim, J. Tsutsui, and S. C. Doney, 2005: Response of the North Atlantic thermohaline circulation and ventilation to increasing carbon dioxide in CCSM3. *J. Climate*, this issue.
- Cobb, K. M., C. D. Charles, H. Cheng, and R. L. Edwards, 2003: El Nino/Southern oscillation and tropical Pacific climate during the last millennium. *Nature*, **424**, 271-276.
- Collins, W. D., M. Blackmon, C. M. Bitz, G. B. Bonan, C. S. Bretherton, J. A. Carton, P. Chang, S. C. Doney, J. J. Hack, J. T. Kiehl, *et al.*, 2005a: The Community Climate System Model: CCSM3. *J. Climate*, this issue.
- Collins, W. D., P. J. Rasch, B. A. Boville, J. J. Hack, J. R. McCaa, D. L. Williamson, B. Briegleb, C. M. Bitz, S.-J. Lin, and M. Zhang, 2005b: The formulation and atmospheric simulation of the Community Atmosphere Model: CAM3. *J. Climate*, this issue.

- Cook, E. R., R. D. D'Arrigo, and M. E. Mann, 2002: A well-verified, multiproxy reconstruction of the winter North Atlantic Oscillation index since A.D. 1400. *J. Climate*, **15**, 1754-1764.
- Crutzen, P. I., 2002: Geology of mankind. *Nature*, **415**, 23.
- Deser, C., M. S. Alexander, and M. S. Timlin, 2003: Understanding the persistence of sea surface temperature anomalies in midlatitudes. *J. Climate*, **16**, 57-72.
- Deser, C., A. Capotondi, R. Saravanan, and A. Phillips, 2005: Tropical Pacific and Atlantic climate variability in CCSM3. *J. Climate*, this issue.
- Dickinson, R. E., K. W. Oleson, G. B. Bonan, F. Hoffman, P. Thornton, M. Vertenstein, Z.-L. Yang, and X. Zeng, 2005: The Community Land Model and its climate statistics as a component of the Community Climate System Model. *J. Climate*, this issue.
- Esper, J., E. R. Cook, and F. H. Schweingruber, 2002: Low-frequency signals in long tree-line chronologies for reconstructing past temperature variability. *Science*, **295**, 2250-2253.
- Gent, P. R., W. G. Large, and F. O. Bryan, 2001: What sets the mean transport through the Drake Passage? *J. Geophys. Res.*, **106**, 2693-2712.
- Gent, P. R., F. O. Bryan, G. Danabasoglu, and K. Lindsay, 2005: Ocean chlorofluorocarbon and heat uptake during the 20th century in the CCSM3. *J. Climate*, this issue.
- Gong, D.-Y. and S.-W. Wang, 1998: Antarctic oscillation: Concept and applications. *Chinese Sci. Bull.*, **43**, 73-738.
- Hack, J. J., J. M. Caron, G. Danabasoglu, K. W. Oleson, C. M. Bitz, and J. E. Truesdale, 2005a: CCSM CAM3 climate simulation sensitivity to changes in horizontal resolution. *J. Climate*, this issue.

- Hack, J. J., J. M. Caron, S. G. Yeager, K. W. Oleson, M. M. Holland, J. E. Truesdale, and P. J. Rasch, 2005b: Simulation of the global hydrological cycle in the CCSM Community Atmosphere Model (CAM3): Mean features. *J. Climate*, this issue.
- Holland, M. M., C. M. Bitz, E. C. Hunke, W. H. Lipscomb, and J. L. Schramm, 2005: Influence of parameterized sea ice thickness distribution on polar climate in CCSM3. *J. Climate*, this issue.
- Huang, S., H. N. Pollack, and P.-Y. Shen, 2000: Temperature trends over the past five centuries reconstructed from borehole temperatures. *Nature*, **403**, 756-758.
- Hurrell, J. W., J. J. Hack, A. Phillips, J. M. Caron, and J. Yin, 2005: The dynamical simulation of the Community Atmosphere Model Version 3 (CAM3). *J. Climate*, this issue.
- Jones, P. D. and M. E. Mann, 2004: Climate over the past millennia. *Rev. Geophys.*, **42**, RG2002, doi:10.1029/2003RG000143.
- Kessler, W. S., 1990: Observations of long Rossby waves in the northern tropical Pacific. *J. Geophys. Res.*, **95**, 5183-5217.
- Kiehl, J. T., C. A. Shields, J. J. Hack, and W. D. Collins, 2005: The climate sensitivity of the Community Climate System Model: CCSM3. *J. Climate*, this issue.
- Lamarque, J.-F., P. Hess, L. Emmons, L. Buja, W. M. Washington, and C. Granier, 2005: Tropospheric ozone evolution between 1890 and 1990. *J. Geophys. Res.*, **110**, D08304, doi:10.1029/2004JD005537.
- Large, W. G. and G. Danabasoglu, 2005: Attribution and impacts of upper ocean biases in CCSM3. *J. Climate*, this issue.

- Otto-Bliesner, B. L. and E. C. Brady, 2001: Tropical Pacific variability in the NCAR Climate System Model. *J. Climate*, **14**, 3587-3607.
- Otto-Bliesner, B. L., E. C. Brady, G. Clauzet, R. Tomas, S. Levis, and Z. Kothavala, 2005: Last Glacial Maximum and Holocene Climate in CCSM3. *J. Climate*, this issue.
- Ramaswamy, V., O. Boucher, J. Haigh, D. Hauglustaine, J. Haywood, G. Myhre, T. Nakajima, G. Y. Shi, and S. Solomon, 2001: Radiative forcing of climate change. *Climate Change 2001: The Scientific Basis. Contribution of Working Group I to the Third Assessment Report of the Intergovernmental Panel on Climate Change*, J. T. Houghton, Y. Ding, D.J. Griggs, M. Noguer, P.J. van der Linden, X. Dai, K. Maskell, and C.A. Johnson, Ed., Cambridge University Press, 881.
- Rasch, P. J., M. C. Barth, J. T. Kiehl, S. E. Schwartz, and C. M. Benkovitz, 2000: A description of the global sulfur cycle and its controlling processes in the National Center for Atmospheric Research Community Climate Model, Version 3. *J. Geophys. Res.*, **105**, 1367-1385.
- Rayner, N. A., D. E. Parker, E. B. Horton, C. K. Folland, L. V. Alexander, D. P. Rowell, E. C. Kent, and A. Kaplan, 2003: Global analyses of sea surface temperature, sea ice, and night marine air temperature since the late nineteenth century. *J. Geophys. Res.*, **108**, 4407, doi:10.1029/2002JD002670.
- Smith, S. J., H. Pitcher, and T. M. L. Wigley, 2001: Global and regional anthropogenic sulfur dioxide emissions. *Global Biogeochemical Cycles*, **29**, 99-119.
- Thompson, D. W. J. and J. M. Wallace, 1998: The Arctic Oscillation signature in the wintertime geopotential height and temperature fields. *Geophys. Res. Lett.*, **25**, 1297-1300.

Urban, F. E., J. E. Cole, and J. T. Overpeck, 2000: Influence of mean climate change on climate variability from a 155-year tropical Pacific coral record. *Nature*, **407**, 989-993.

Wang, W.-C., X.-Z. Liang, M. P. Dudek, D. Pollard, and S. L. Thompson, 1995: Atmospheric ozone as a climate gas. *Atmospheric Research*, **37**, 247-256.

Whitworth, T. and R. Peterson, 1985: Volume transport of the Antarctic Circumpolar Current from bottom water measurements. *J. Phys. Oceanogr.*, **15**, 810-816.

Yeager, S. G., W. G. Large, J. J. Hack, and C. A. Shields, 2005: The low resolution CCSM3. *J. Climate*, this issue.

## Figure legends

Fig. 1. Zonally-averaged annual surface temperature changes ( $^{\circ}\text{C}$ ), PI minus PD, for the T31x3 and T42x1 coupled and T42-SOM CCSM3 simulations.

Fig. 2. Mean annual precipitation (mm/day) for PI simulations, T42x1 (top) and T31x3 (middle). Zonally-averaged annual precipitation changes (mm/day), PI minus PD, for the T31x3 and T42x1 coupled simulations (bottom).

Fig. 3. Mean DJF and JJA sea level pressure (mb) for PI simulations. Contour interval is 4 hPa.

Fig. 4. Mean annual potential temperature ( $^{\circ}\text{C}$ ) along the Equator as a function of depth and longitude for PI simulations (top) and difference, PI minus PD (bottom).

Fig. 5. Mean annual meridional overturning streamfunction in the Atlantic basin for the T42x1 PI simulation (top) and T31x3 simulation (bottom). Contours of the mean streamfunction are overlaid with the PI-PD difference in color. Contour interval of the mean streamfunction is 2.5 Sverdrups. Color bar indicates values of the differences shown.

Fig. 6. Latitudinal profile of northward ocean heat transport by the mean Eulerian advection for the Atlantic basin for the PI and PD simulations at T42x1 and T31x3 resolutions.

Fig. 7. CCSM3 ice thickness in meters (filled color contours) for February-March and August-September for the T42x1 and T31x3 PI simulations. Values less than 0.25 m are not colored. The differences from the PD simulation are shown as black line contours, negative values are dashed, the contour interval is 0.5 m, and zero contours are omitted.

Fig. 8. The seasonal cycle of the aggregate ice area for the PI and PD simulations at T42x1 and T31x3 resolutions.

Fig. 9. Monthly standard deviations of the Niño3.4 SST indices for the T42x1 PD, T42x1 PI, T31x3 PD, and T31x3 PI simulations.

Fig. 10. Arctic Oscillation simulated by the PI simulations of the T42x1 and T31x3 coupled and the T42-SOM CCSM3 models. Shown are the regressions of sea level pressure anomalies (top) and surface temperature (middle) on the leading principal component time series of the winter (December-March) mean sea level pressure anomalies over the Northern Hemisphere (20-90°N). Bottom panel shows power spectra of leading principal component time series. See text for discussion of significance of spectra.

Fig. 11. Southern Annular Mode simulated by the PI simulations of the T42x1 and T31x3 coupled and the T42-SOM CCSM3 models. Shown are the regressions of sea level pressure anomalies (top) and surface temperature (middle) on the leading principal component time series of the monthly mean sea level pressure anomalies over the Southern Hemisphere (20-

90°S). Bottom panel shows power spectra of leading principal component time series. See text for discussion of significance of spectra.

### **Table Captions**

Table 1. Forcings changed in the PI simulations from their specifications in the PD simulations.

Table 2. Annual mean and standard deviations (parentheses) for CCSM3 simulations for PI and PD at T42x1 and T31x3 resolutions.

Table 3. Ocean statistics for the PI and PD simulations at T42x1 and T31x3 resolutions

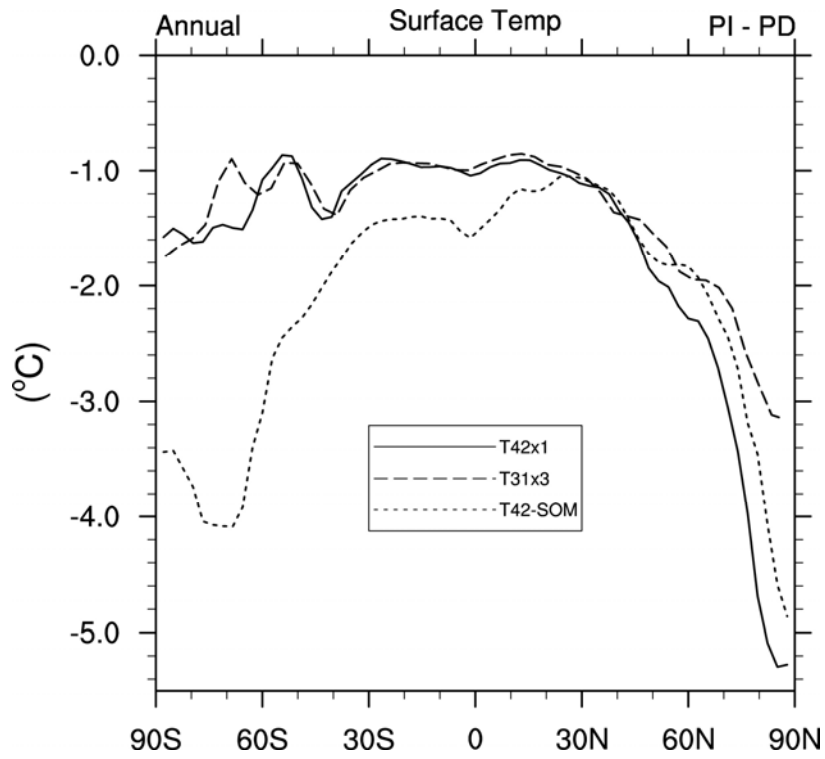


Fig. 1. Zonally-averaged annual surface temperature changes ( $^{\circ}\text{C}$ ), PI minus PD, for the T31x3 and T42x1 coupled and T42-SOM CCSM3 simulations.

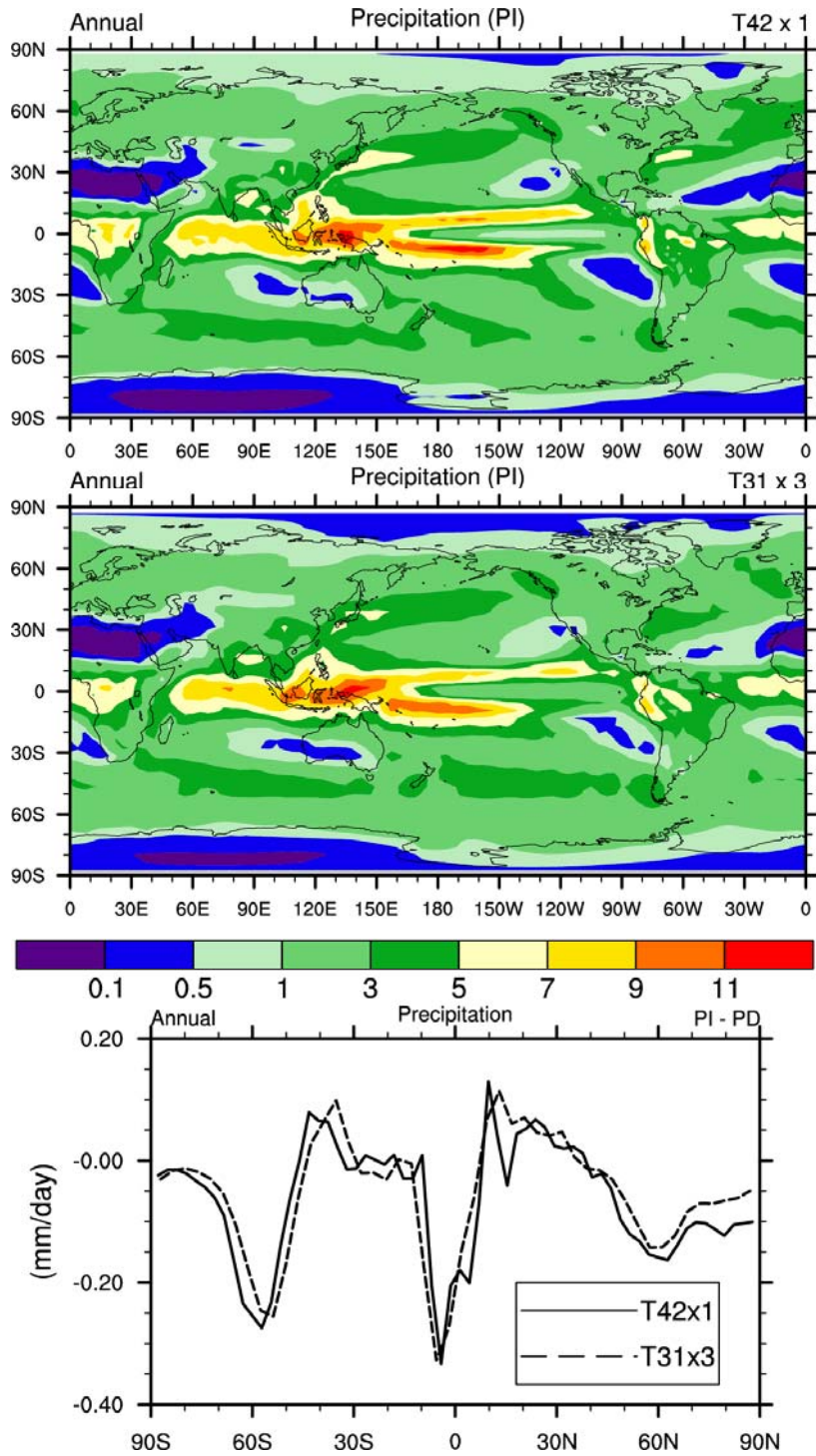


Fig. 2. Mean annual precipitation (mm/day) for PI simulations, T42x1 (top) and T31x3 (middle). Zonally-averaged annual precipitation changes (mm/day), PI minus PD, for the T31x3 and T42x1 coupled simulations (bottom).

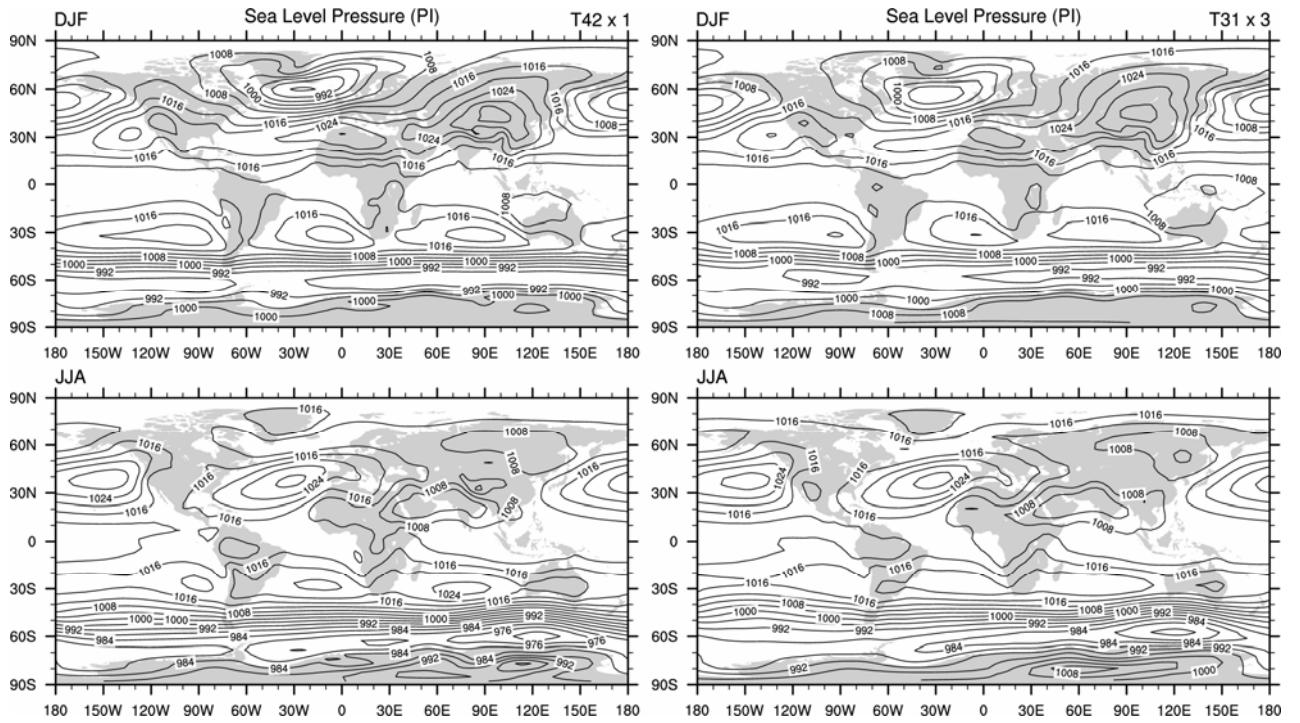


Fig. 3. Mean DJF and JJA sea level pressure (mb) for PI simulations. Contour interval is 4 hPa.

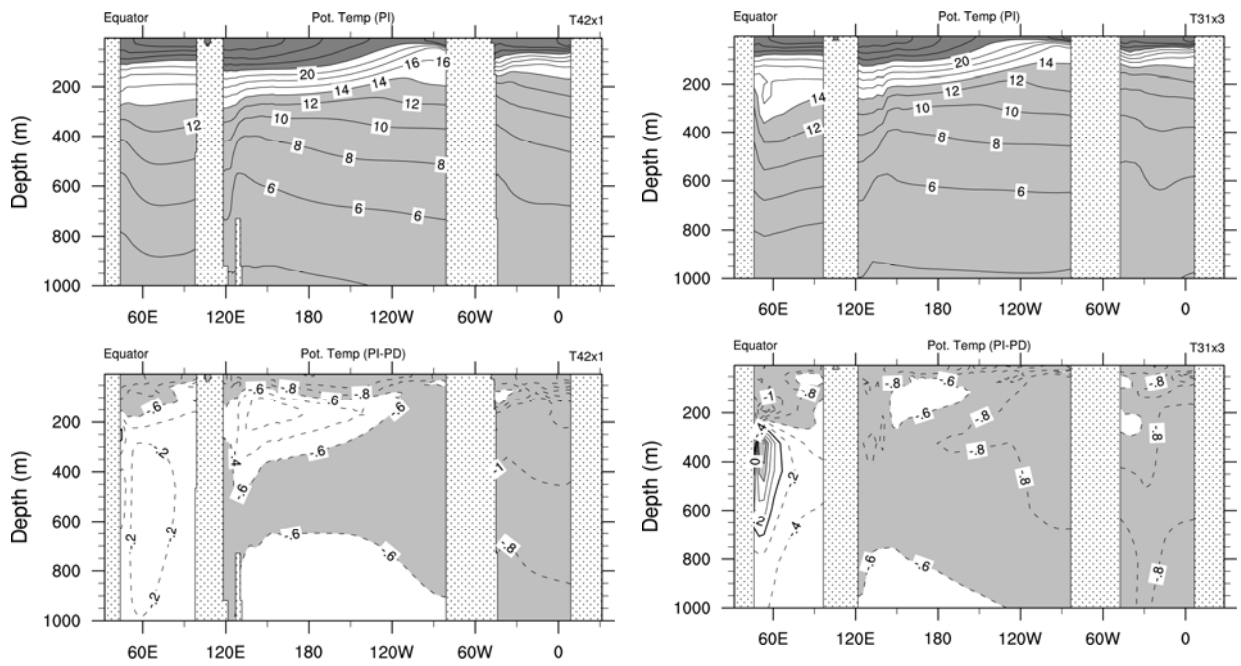


Fig. 4. Mean annual potential temperature ( $^{\circ}\text{C}$ ) along the Equator as a function of depth and longitude for PI simulations (top) and difference, PI minus PD (bottom).

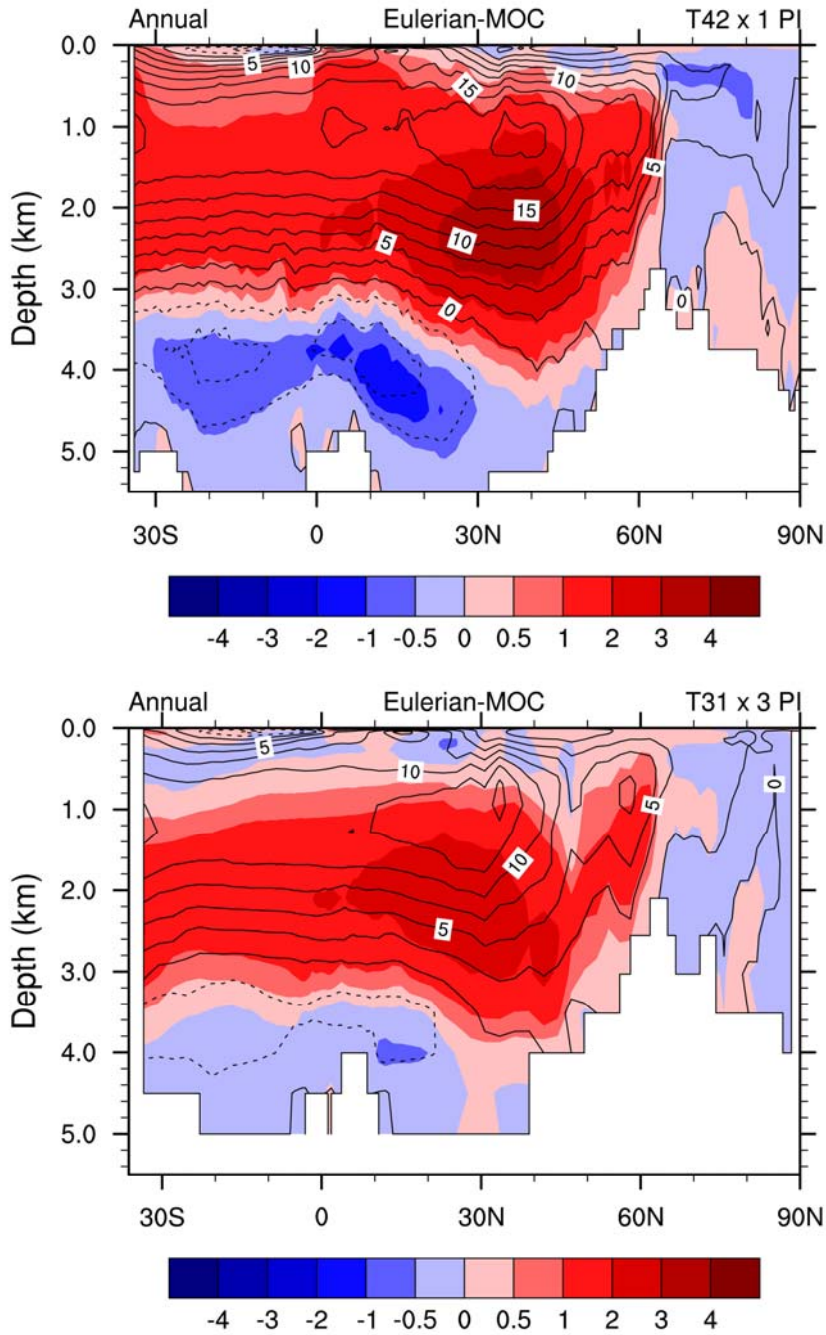


Fig. 5. Mean annual meridional overturning streamfunction in the Atlantic basin for the T42x1 PI simulation (top) and T31x3 simulation (bottom). Contours of the mean streamfunction are overlaid with the PI-PD difference in color. Contour interval of the mean streamfunction is 2.5 Sverdrups. Color bar indicates values of the differences shown.

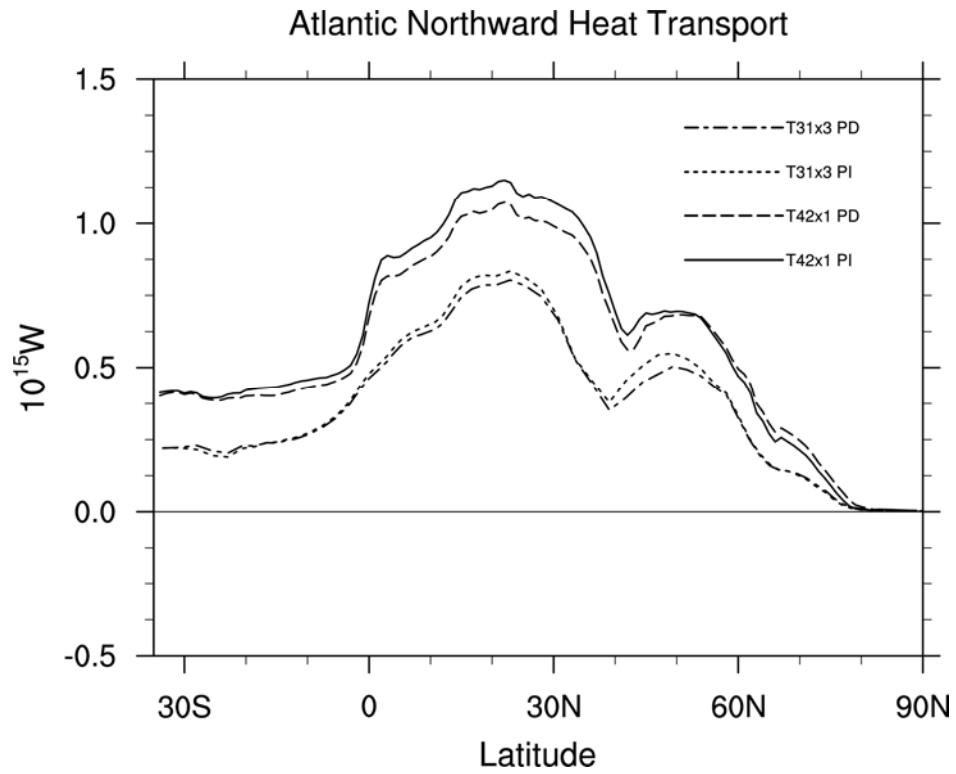


Fig. 6. Latitudinal profile of northward ocean heat transport by the mean Eulerian advection for the Atlantic basin for the PI and PD simulations at T42x1 and T31x3 resolutions.

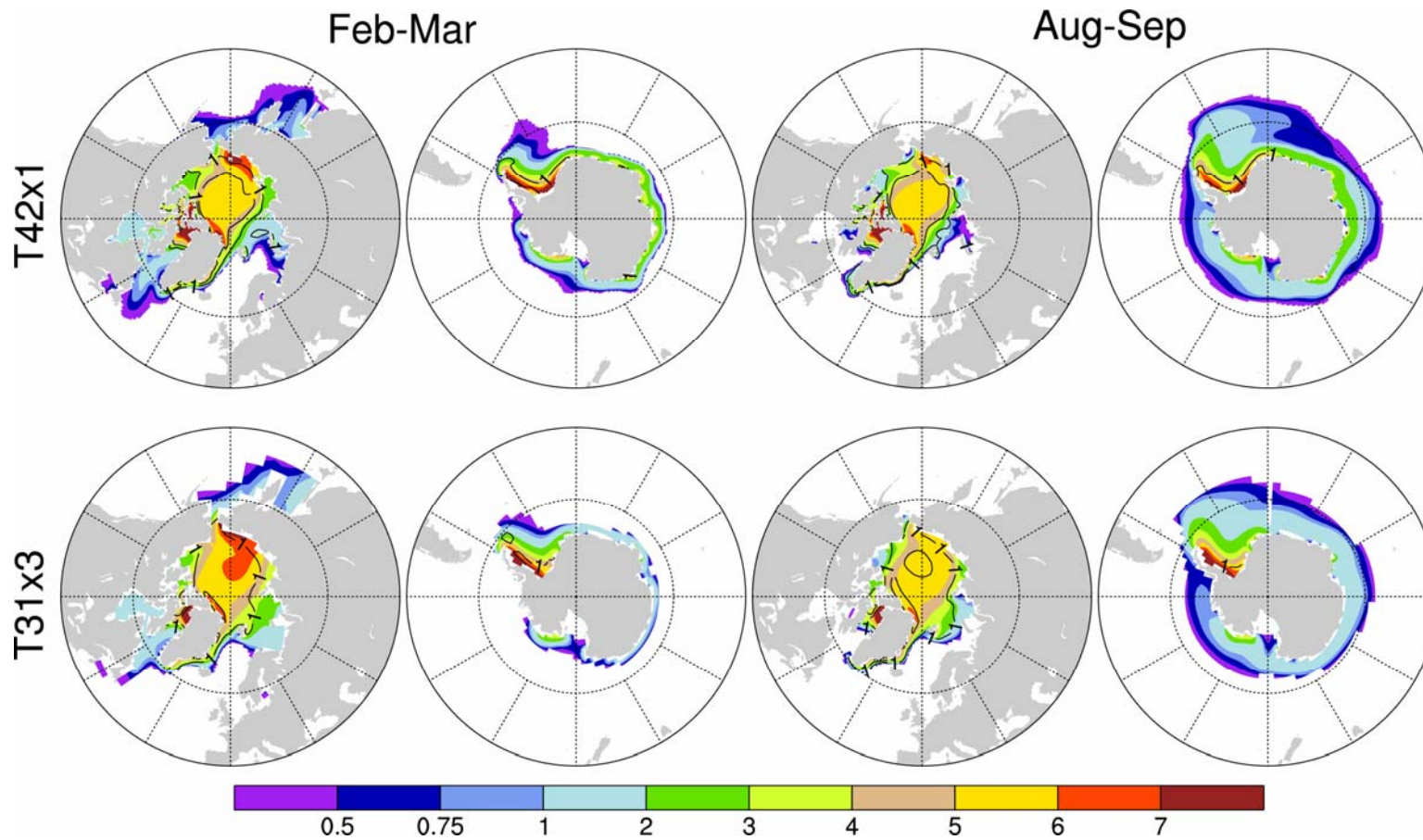


Fig. 7. CCSM3 ice thickness in meters (filled color contours) for February-March and August-September for the T42x1 and T31x3 PI simulations. Values less than 0.25 m are not colored. The differences from the PD simulation are shown as black line contours, negative values are dashed, the contour interval is 0.5 m, and the zero contour is omitted.

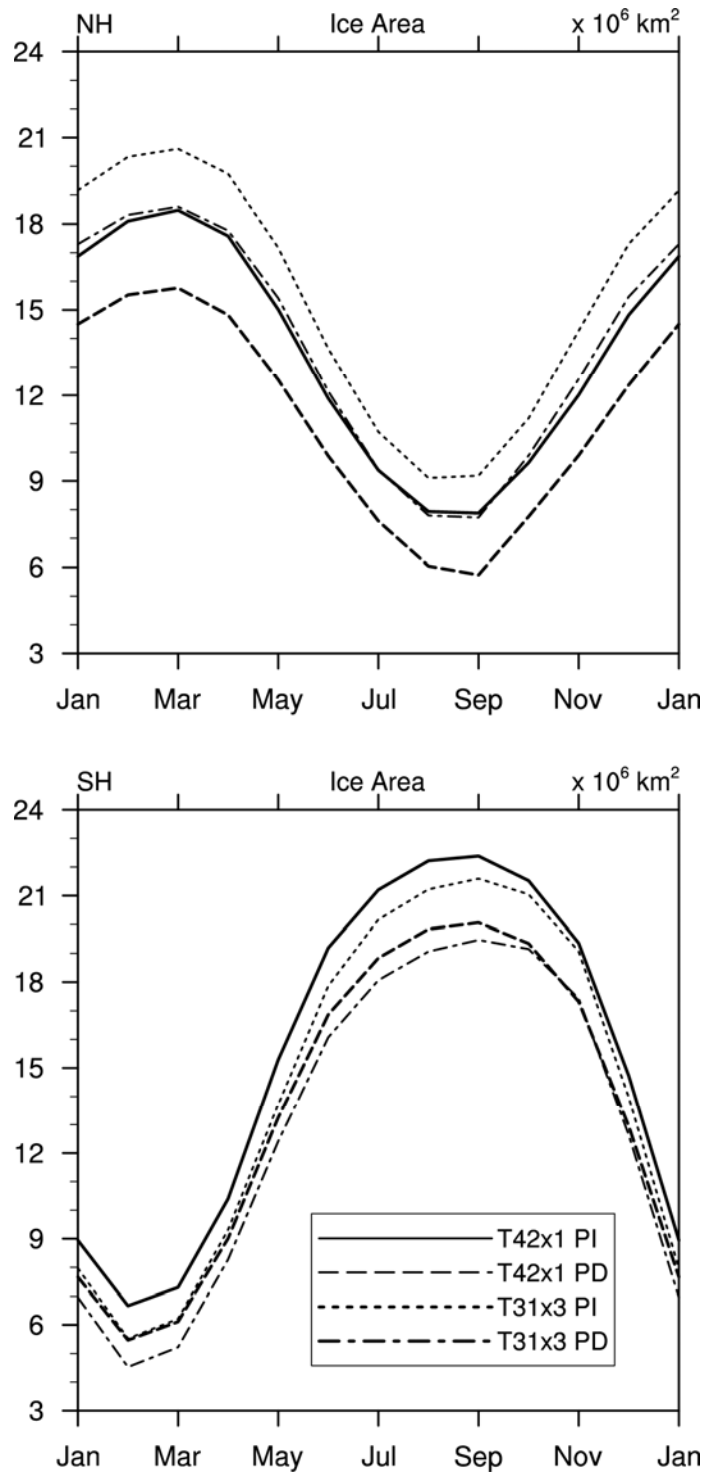


Fig. 8. The seasonal cycle of the aggregate ice area for the PI and PD simulations at T42x1 and T31x3 resolutions.

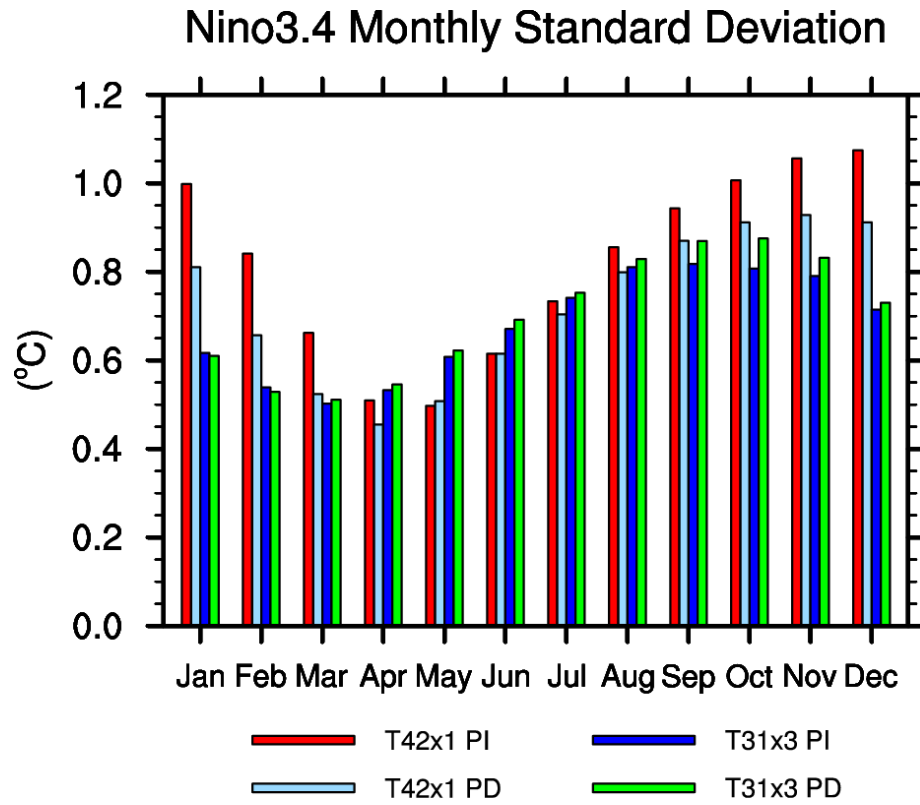


Fig. 9. Monthly standard deviations of the Niño3.4 SST indices for the T42x1 PD, T42x1 PI, T31x3 PD, and T31x3 PI simulations.

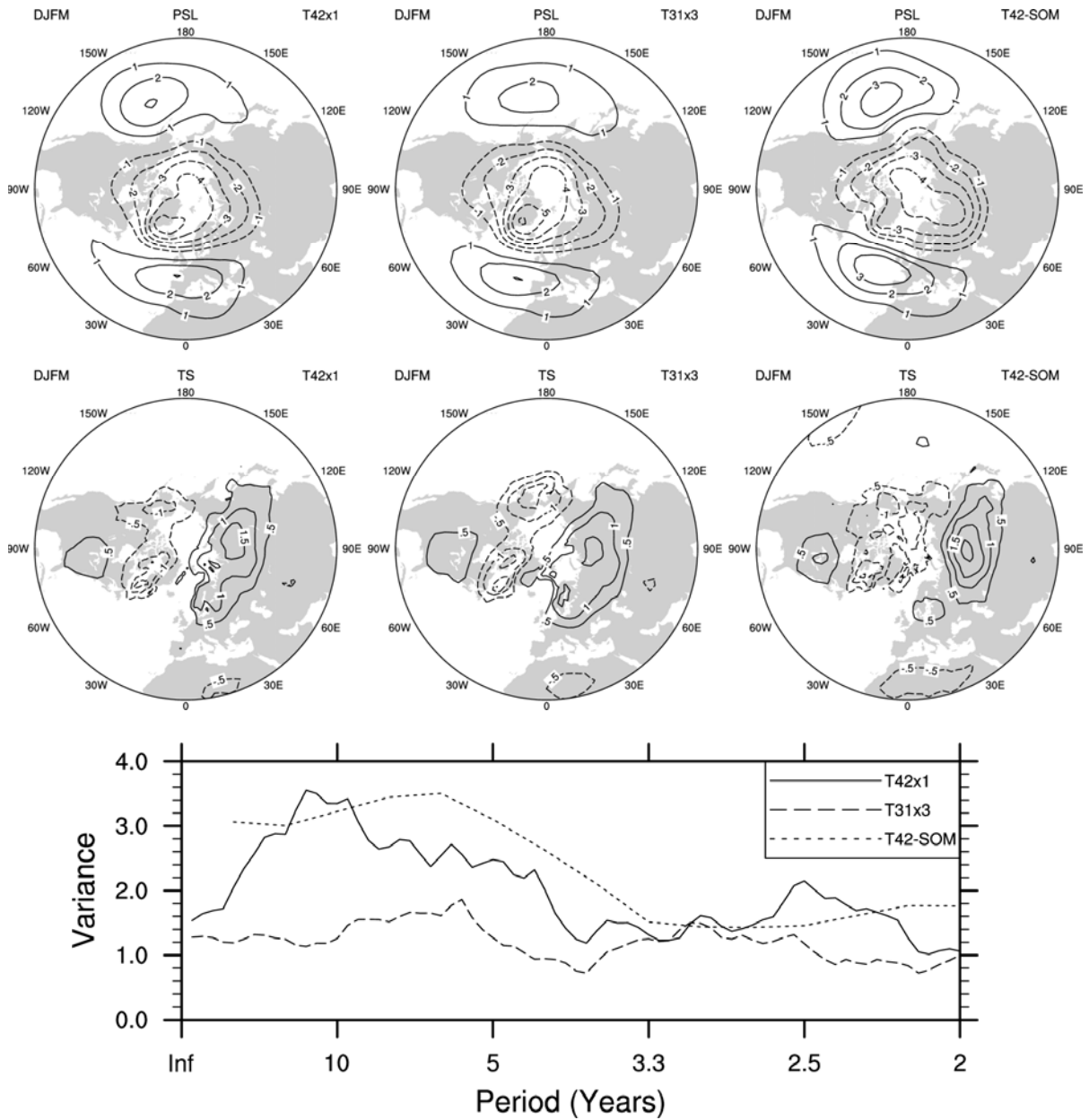


Fig. 10. Arctic Oscillation simulated by the PI simulations of the T42x1 and T31x3 coupled and the T42-SOM CCSM3 models. Shown are the regressions of sea level pressure anomalies (top) and surface temperature (middle) on the leading principal component time series of the winter (December-March) mean sea level pressure anomalies over the Northern Hemisphere (20-90°N). Bottom panel shows power spectra of leading principal component time series. See text for discussion of significance of spectra.

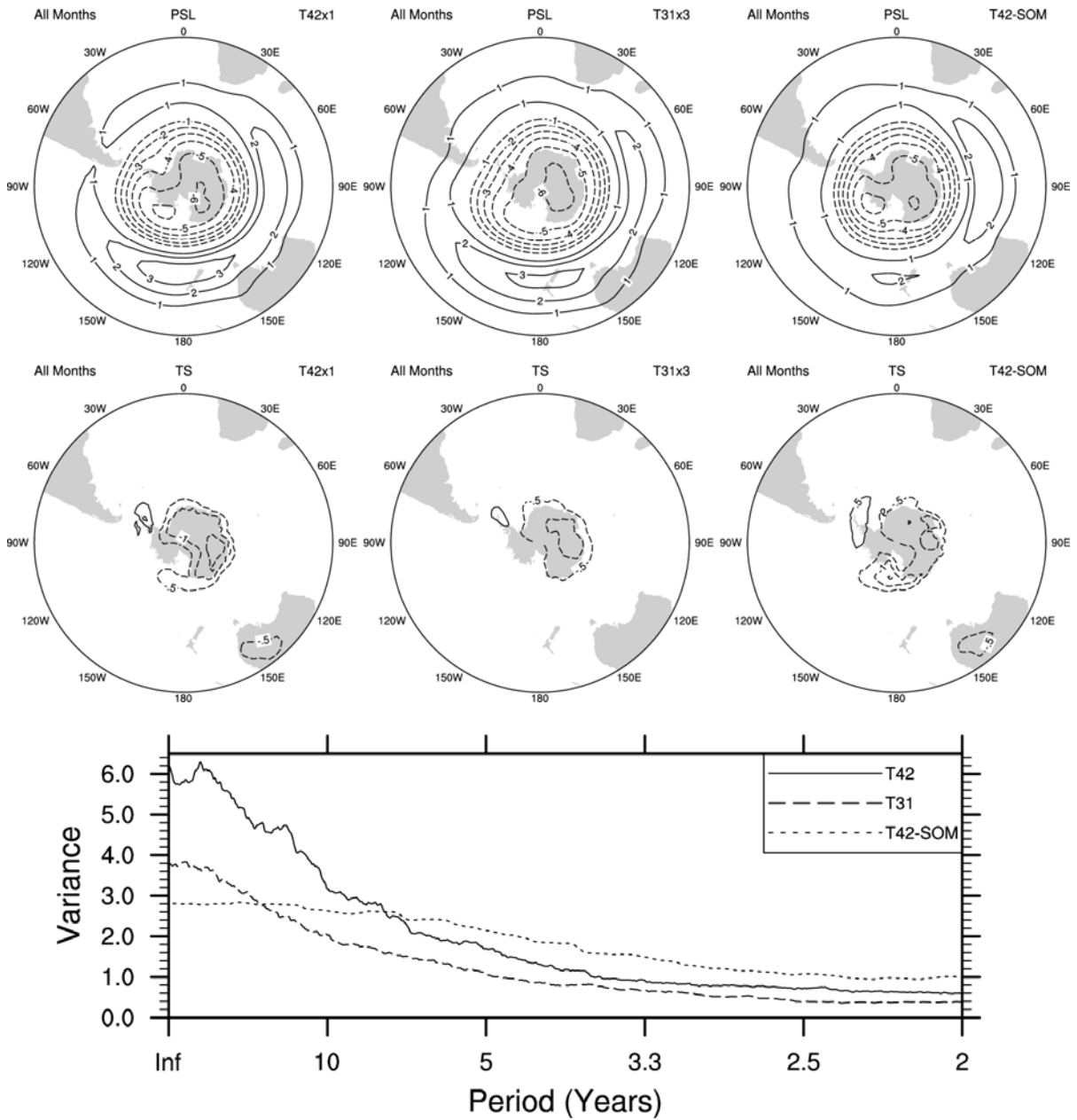


Fig. 11. Southern Annular Mode simulated by the PI simulations of the T42x1 and T31x3 coupled and the T42-SOM CCSM3 models. Shown are the regressions of sea level pressure anomalies (top) and surface temperature (middle) on the leading principal component time series of the monthly mean sea level pressure anomalies over the Southern Hemisphere (20-90°S). Bottom panel shows power spectra of leading principal component time series. See text for discussion of significance of spectra.

<b>Forcing</b>	<b>PI</b>	<b>PD</b>
CO <sub>2</sub>	280x10 <sup>-6</sup>	355x10 <sup>-6</sup>
CH <sub>4</sub>	760x10 <sup>-9</sup>	1714x10 <sup>-9</sup>
N <sub>2</sub> O	270x10 <sup>-9</sup>	311x10 <sup>-9</sup>
F11	0	30x10 <sup>-12</sup>
F12	0	50.3x10 <sup>-12</sup>
O <sub>3</sub>	1870 AD	Present Day
Sulfate Aerosols	1870 AD	Present Day
Dust and Sea Salt	Present Day	Present Day
Carbonaceous Aerosols	30% of Present Day	Present Day
Solar Constant	1365 Wm <sup>-2</sup>	1367 Wm <sup>-2</sup>
Orbital Year	1950 AD	1990 AD

All trace gases are expressed as volume mixing ratios. Orbital year for PI is specified to be 1950 AD from the PMIP-2 experimental design. Land-use is fixed at present-day for all simulations.

Table 1. Forcings changed in the PI simulations from their specifications in the PD simulations.

	<b>T42x1</b>		<b>T31x3</b>	
	<b>Preind</b>	<b>Present</b>	<b>Preind</b>	<b>Present</b>
<b>Global</b>				
Surface Net Longwave Flux ( $W m^{-2}$ )	58.95 (0.18)	56.86 (0.18)	58.72 (0.19)	56.65 (0.17)
Surface Net Shortwave Flux ( $W m^{-2}$ )	160.11 (0.28)	158.72 (0.26)	160.29 (0.28)	158.75 (0.27)
Surface Latent Heat Flux ( $W m^{-2}$ )	79.99 (0.24)	81.48 (0.24)	77.58 (0.21)	78.91 (0.20)
Precipitation (mm/day)	2.74 (0.01)	2.79 (0.01)	2.66 (0.01)	2.70 (0.01)
Precipitation - Land (mm/day)	2.02 (0.03)	2.07 (0.03)	1.91 (0.03)	1.96 (0.03)
Precipitation- Ocean (mm/day)	3.22 (0.01)	3.25 (0.01)	3.18 (0.01)	3.21 (0.01)
Precipitable Water (mm)	22.19 (0.11)	24.13 (0.12)	20.53 (0.11)	22.30 (0.12)
Surface Sensible Heat Flux ( $W m^{-2}$ )	21.69 (0.10)	20.60 (0.12)	24.39 (0.09)	23.23 (0.12)
Snow Depth Water Equiv (cm)	9.49 (0.05)	9.17 (0.05)	9.03 (0.07)	8.83 (0.06)
Surface Temperature ( $^{\circ}C$ )	13.52 (0.08)	14.80 (0.06)	12.83 (0.09)	14.01 (0.08)
<b>Tropics (20°S-20°N)</b>				
Sea Surface Temperature ( $^{\circ}C$ )	26.58 (0.07)	27.48 (0.11)	26.34 (0.12)	27.20 (0.14)
Surface Temperature - Land ( $^{\circ}C$ )	24.66 (0.11)	25.84 (0.15)	24.12 (0.16)	25.28 (0.19)
<b>Extratropics (20-90°)</b>				
Southern Ocean SST	5.89 (0.09)	6.71 (0.04)	6.12 (0.08)	6.94 (0.04)
GIN Sea SST	4.32 (0.27)	5.54 (0.26)	1.24 (0.48)	1.72 (0.54)
Labrador Sea SST	-0.17 (0.30)	0.83 (0.31)	-0.64 (0.16)	-0.09 (0.21)
SH Sea Ice Area ( $10^6 km^2$ )	16.01 (0.53)	13.94 (0.35)	15.08 (0.37)	13.20 (0.37)
NH Sea Ice Area ( $10^6 km^2$ )	13.35 (0.33)	11.07 (0.25)	15.07 (0.47)	13.60 (0.26)

Table 2. Annual mean and standard deviations (parentheses) for CCSM3 simulations for PI and PD at T42x1 and T31x3 resolutions.

	<b>T42x1</b>		<b>T31x3</b>	
	<b>Preindustrial</b>	<b>Present</b>	<b>Preindustrial</b>	<b>Present</b>
<b>Ocean Transports (Sv)</b>				
Drake Passage	195.13 (3.23)	179.13 (2.83)	113.92 (2.87)	113.62 (2.73)
Pac. Ind. Throughflow	-18.04 (1.43)	-16.32 (1.24)	-11.20 (0.74)	-10.64 (0.80)
Florida Straits	28.30 (0.78)	27.99 (0.86)	17.50 (1.16)	16.31 (1.00)
Bering Strait	0.93 (0.24)	0.90 (0.28)	0.52 (0.16)	0.45 (0.16)
<b>Atlantic Overturning (Sv)</b>				
Max NADW	21.0 @1022m	19.0 @1022m	15.9 @944m	15.1 @686m
Max ABW (34°S)	-4.2 @3750m	-3.8 @3750m	-3.7 @3516m	-4.0 @3516m
<b>Niño 3.4 Statistics (°C)</b>				
Standard Deviation	0.84	0.74	0.69	0.71
Min	0.50	0.45	0.51	0.51
Max	1.07	0.93	0.82	0.87

The averages of barotropic transport within key straits are computed over the last 100 years of model integrations. Mean Atlantic overturning streamfunction is computed over a 50-year period and represents the streamfunction due to the mean Eulerian flow. Niño3.4 averages are computed over the last 350 years of integration after removal of annual cycle and smoothing with a 5-month boxcar filter.

Table 3. Means and standard deviations (in parentheses) for the ocean in the PI and PD simulations at T42x1 and T31x3 resolutions.